Influence of Structural Defects on Biomineralized ZnS Nanoparticle Dissolution: An In-Situ Electron Microscopy Study

Jeremy R. Eskelsen[a], Jie Xu[b], Michelle Chiu[a], Ji-Won Moon[c], Branford Wilkins[a], David E. Graham[c], Baohua Gu[a], Eric M. Pierce[a‡*]

[a]Environmental Sciences Division, Oak Ridge National Laboratory, P.O. Box 2008, MS 6038, Oak Ridge, TN 37831

[b]Geological Sciences, University of Texas at El Paso, 500 West University Ave, El Paso, TX 79968

[c]Biosciences Division, Oak Ridge National Laboratory, P.O. Box 2008, MS 6038, Oak Ridge, TN 37831

KEYWORDS[1]**:** liquid cell electron microscopy, metal sulfides, nanoparticles, dissolution, structural defect, sphalerite, zinc blende, wurtzite.

*Corresponding Author: Eric M. Pierce

Phone: (865) 574-9968

Fax: (865) 576-8646

Email: pierceem@ornl.gov

ABSTRACT: The dissolution of metal sulfides, such as ZnS, is an important biogeochemical process affecting fate and transport of trace metals in the environment. However, currently studies of in-situ dissolution of metal sulfides and the effects of structural defects on dissolution are lacking. Here we have examined the dissolution behavior of ZnS nanoparticles synthesized via several abiotic and biological pathways. Specifically, the biogenic ZnS nanoparticles were produced by an anaerobic, metal-reducing bacterium *Thermoanaerobacter* sp. X513 in a Zn-amended, thiosulfate-containing growth medium either in the presence or absence of silver (Ag), whereas the abiogenic ZnS nanoparticles were produced by mixing an aqueous Zn solution with either H_2S-rich gas or Na_2S solution. The size distribution, crystal structure, aggregation behavior, and internal defects of the synthesized ZnS nanoparticles were examined using high-resolution transmission electron microscopy (TEM) coupled with X-ray energy dispersive spectroscopy. The characterization results show that both the biogenic and abiogenic samples were dominantly composed of sphalerite. In the absence of Ag, the biogenic ZnS nanoparticles were significantly larger (i.e., ~10 nm) than the abiogenic ones (i.e., ~3–5 nm) and contained structural defects (e.g., twins and stacking faults). The presence of trace Ag showed a restraining effect on the particle size of the biogenic ZnS, resulting in quantum-dot-sized nanoparticles (i.e., ~3 nm). In situ dissolution experiments for the synthesized ZnS were conducted with a liquid-cell TEM (LCTEM), and the primary factors (i.e., the presence or absence structural defects) were evaluated for their effects on the dissolution behavior using the biogenic and abiogenic ZnS nanoparticle samples with the largest average particle size. Analysis of the dissolution results (i.e., change in particle radius with time) using the Kelvin equation shows that the defect-bearing biogenic ZnS nanoparticles (γ = 0.799 J/m^2) have a significantly higher surface energy than the abiogenic ZnS nanoparticles (γ = 0.277 J/m^2). Larger defect-bearing biogenic ZnS nanoparticles

were thus more reactive than the smaller quantum-dot-sized ZnS nanoparticles. These findings provide new insight into the factors that affect the dissolution of metal sulfide nanoparticles in relevant natural and engineered scenarios, and have important implications for tracking the fate and transport of sulfide nanoparticles and associated metal ions in the environment. Moreover, our study exemplified the use of an in-situ method (i.e., LCTEM) to investigate nanoparticle behavior (e.g., dissolution) in aqueous solutions.

INTRODUCTION

Solid–fluid interfacial reactions that govern the formation of fine-grained nanoparticulate metal sulfides have relevance to a range of areas with energy and industrial applications (e.g., sedimentary sulfide ore deposit formation, geochemical cycling of elements in the earth's crust, contaminated site remediation, and semiconductor research).[1, 2] From an environmental perspective, the influence that the formation of fine-grained metal sulfides can have on the world's aquatic resources and the geochemical cycling of elements cannot be overstated. For example, the bioavailability and transport of metals ions (e.g., Fe, Zn, and Hg) in anoxic environments—such as marine ecosystems near hydrothermal vents, stream biofilms, acid mine drainage, and the pores of anaerobic sediments—is directly controlled by the production of sulfides by sulfate-reducing bacteria.[3-9] Sulfate-reducing bacteria are ubiquitous in natural systems, where they obtain electrons by oxidizing organic carbon compounds to reduce sulfate to sulfide, which is the dominant process for sulfide production in low-temperature (<100 °C) environments.[10] Furthermore, recognition that nanoparticulate biogenic metal sulfides, such as zinc sulfide (ZnS) and mercury sulfide, can persist in oxic waters for months, transporting metals to other ecosystem compartments, has broad interest; the process is influenced in part by the

nanoparticles' size-dependent properties (e.g., surface free energy) and their interaction with dissolved organic molecules, which can serve as capping agents.[11-16] For example, Priadi et al.[16] reported that amorphous ZnS nanoparticles became a dominant form of zinc in the Seine River downstream sections, thereby controlling the partitioning of this trace metal between suspended particles and aqueous solution. Thus, developing a detailed understanding of the mechanisms that govern the growth and dissolution of biogenic sulfides (e.g., ZnS, mercury sulfide [HgS], cadmium sulfide [CdS], etc.) is of interest to a range of scientific disciplines, including low temperature geochemistry, microbial ecology, environmental engineering, and materials science. Here we use ZnS as a model system to investigate the relationship that exist between nanoparticle dissolution rates and their morphology and crystal structure. Zinc sulfide was chosen due to its relevance for biogeochemical cycles and industrial applications, as well as their exclusive monosulfide phase (i.e., one oxidation state of zinc and one oxidation state for sulfur), which allows us to focus on the nanoparticles' morphology and crystal structure attributes. Furthermore, the ZnS crystal structure is similar to a wide range of environmentally important metal sulfides, such as CdS and HgS, and is expected to behave similarly during nanoparticle growth and dissolution.[17]

The crystallization and growth of ZnS nanoparticles are initiated by the formation of small soluble complexes [$Zn_3S_3(H_2O)_6$ rings] ~7 Å in size that grow to ~9.7 Å by cross-linking to form nanoscale clusters [i.e., $Zn_4S_6(H_2O)_4^{-4}$ or $Zn_6S_4(H_2O)_4^{-4}$] that are structurally similar to sphalerite.[18-23] When nucleation rates are high and growth rates are slow, nanoparticle crystallites persist, especially in the presence of capping agents. For example, capping agents have been used to synthesize ZnS nanocrystals for optical applications, and it has been demonstrated in controlled laboratory conditions that small thiol-complexes can also serve a similar role as a

capping agent for ZnS nanoparticles that form in the natural systems [12, 13] Such thiol complexes persist in anaerobic transition zone porewaters where metal sulfides form, such as at the groundwater–surface water interface, in wetlands, and in the anaerobic zones of biofilms.[6, 24-26]

Following the initial nucleation event where ions and molecules crystallize to form nanoparticles, particle growth can occur via two processes (1) classical growth via an Ostwald ripening (OR) and/or LaMer mechanism and (2) non-classical growth via an oriented attachment mechanism (OA) (i.e., cluster growth).[27] The classical growth process occurs when smaller unstable particles dissolve and their dissolved components diffuse and support the growth of larger nanoparticles.[28, 29] The non-classical growth process (OA) proceeds from the joining of two or more interacting nuclei or crystallites to form a larger nanoparticle.[30] The OA mechanism has been proposed to play an important role in the formation of defects, such as twin boundaries, stacking faults, and dislocations. Both of the aforementioned mechanisms are critical steps in nanoparticle growth, with the OA mechanisms being known to occur first for some materials followed by an OR process when the aqueous condition is tightly controlled.[31] The presence or absence of additional solutes in the aqueous solution during nanoparticle formation serves a key function in controlling the surface reactivity and shape of nanoparticles.[31, 32] For example, often in quantum dot nanoparticle synthesis, capping agents are utilized to physically separate the nanoparticles, to stabilize the small particles, and to inhibit particle–particle fusion (OA).[33] The role of additional solutes in aqueous solutions can be classed into three types of OA conditions: inhibiting, neutral, and promoting. Inhibiting solutions contain components such as capping agents or, in the case of metal sulfides, metal impurities that favor stronger sulfide interactions over the primary medium to disrupt OA by physical separation or modification of the surface structure/composition. Neutral solutions are those that are devoid of additional impurities, thus

enabling OA to occur naturally. Promoting solutions contain reactive agents that enhance particle–particle interactions and thus facilitate the arrangement of nanoparticles close together, thereby increasing the likelihood for OA. Previous studies on ZnS have focused primarily on nanoparticle formation, aggregation, and stability, instead of focusing on understanding how growth mechanisms influence dissolution. One approach to improving our understanding of the role of structural defects and capping agents on ZnS dissolution is to conduct beam-induced dissolution experiments using *in situ* liquid cell transmission electron microscopy (LCTEM). Liquid cell TEM has been used to investigate the formation and aggregation of nanoparticles in real time under aqueous environments.[34, 35] Studies that focus on precipitation of nanostructures by ionic interactions and metal reduction are being conducted by various groups.[36] Some studies have focused on dissolution experiments of the oxidative etching of palladium nanocrystals, while theoretical modeling of chemical pathways under ionization by the electron beam has also been investigated.[37, 38]

The primary objectives of this study were to elucidate how crystal growth conditions and the presence or absence of defects influence ZnS nanoparticle dissolution behavior. To this end, we conducted first-of-their-kind beam-induced LCTEM experiments with both biogenic and abiotic ZnS nanoparticles produced under different OA conditions, specifically neutral and promotion, and related the observed dissolution behavior to changes in surface free energy.

EXPERIMENTAL

Synthesis of ZnS Nanoparticle Samples. Four samples of nanoparticulate ZnS were synthesized using either abiotic or biotic techniques. We briefly describe the synthesis of each sample below. For additional details see the Supporting Information and Moon et al.[39, 40].

Abiogenic ZnS. Two abiotic samples, referred to as abio-ZnS1 and abio-ZnS2, were synthesized from different sulfide sources under oxic and anoxic conditions. The first, abio-ZnS1, was synthesized under oxic conditions by rapidly mixing aqueous solutions of $ZnCl_2$ (0.5 mM) and Na_2S (0.5 mM). Stock solutions of $ZnCl_2$ (4.7 mM) and Na_2S (4.7 mM) were prepared by dissolving analytical-grade $ZnCl_2$ crystals and pre-rinsed Na_2S crystals in deionized water (18.2 MΩ/cm^2 resistivity). A serial dilution of each stock solution was used to prepare the $ZnCl_2$ and Na_2S sample solutions, which were then mixed, sealed, and allowed to react for more than 10 days in the dark to prevent photooxidation of the surface sulfides of the produced ZnS nanoparticles by dissolved O_2 during nanoparticle formation.[41, 42]

The second abiotic ZnS sample (abio-ZnS2) was prepared by mixing H_2S containing-gas with an anoxic solution of 1 M zinc acetate. The gas mixture was microbially produced by a thermophilic bacterial culture (*Thermoanaerobacter* sp. X513) grown in a medium that contained a 6 mM thiosulfate source. The gases present in the headspace (including H_2S) were transferred from the bioreactor by sparging N_2 carrier gas into the bioreactor solution medium, followed by the vent gas mixture flowing through a tube connecting the bioreactor and the zinc acetate solution container.

Biogenic ZnS. Two biotic ZnS samples, referred to as bio-ZnS1 and bio-ZnS2, were extracellularly synthesized in the absence (bio-ZnS1) and presence (bio-ZnS2) of traces of silver (Ag) using the metal-reducing thermophilic bacterium *Thermoanaerobacter* sp. X513.[43] Details of the synthesis and media used in this study are described briefly in the Supplemental Information. For additional details on the synthesis and media see Moon et al. [39, 40]. The source of the Zn used was 5 mM $ZnCl_2$ and 4.5 mM $ZnCl_2$:0.5 mM $AgNO_3$ for bio-ZnS1 and bio-ZnS2 samples, respectively, and the sulfur source was 5.33 mM thiosulfate. After 48 h of incubation at

65 °C with 2 vol % mid-log growth phase cells, anoxic $ZnCl_2$ solution and the $ZnCl_2$:$AgNO_3$ solution mixtures were added drop wise (<2 mL per minute) to a 900 L and 100 L vessel, respectively. The resulting ZnS nanoparticles from the bio-ZnS1 and bio-ZnS2 samples were collected after 24 h of reacting and were repeatedly washed by continuously suspending and centrifuging the sample.

Characterization of ZnS Nanoparticle Samples. As-prepared samples were characterized by X-ray diffraction (XRD), Fourier-transform infrared spectroscopy (FTIR), field-emission scanning electron microscopy (FESEM), transmission electron microscopy (TEM), high-resolution TEM (HRTEM), selected area electron diffraction (SAED), and electron energy loss spectroscopy (EELS). The XRD and FTIR results for abio-ZnS2, bio-ZnS1, and bio-ZnS2 are described elsewhere.[39, 40, 44] Details of the TEM, scanning TEM, and X-ray energy dispersive spectroscopy (EDS) techniques are provided in the Supporting Information.

Liquid Cell Transmission Electron Microscopy. LCTEM was performed on a Hitachi HF-3300 S/TEM using a Protochips Poseidon 200 liquid flow holder (SI Fig. S1). A small bottom E-chip (Protochips) containing a silicon nitride window with 4 × 8 microwells (20 μm × 20 μm × 0.17 μm with no spacer) or 8 × 16 microwells (10 μm × 10 μm × 0.170 μm) and a large chip containing a single silicon nitride window (550 μm × 20 μm) were used to create a static liquid environment in the STEM. The microwell bottom windows and the narrow window of the large chip were chosen to minimize window bowing in the vacuum environment of the STEM. This played an important role in obtaining higher resolution images in STEM mode. The liquid cell holder was argon plasma cleaned for 5 minutes in a Fischione plasma cleaner with the E-chips and O-rings removed. The E-chips were soaked in acetone for about 1 minute, then soaked in methanol for 1 minute. The chips were then removed from the methanol and dried on a paper

filter membrane. Care was taken to ensure the last of the methanol did not dry directly on the windows. A paper filter membrane cut into a wedge was used to carefully wick the methanol away from the window when needed. The chips were placed on a cleaned glass slide and plasma cleaned for about 1 minute (3 × 20 second intervals using a controlled amount of room air as the gas source) in a Harrick model PDC-32G plasma cleaner on the high setting to create a hydrophilic surface on the silicon nitride membranes. The O-rings were carefully cleaned and loaded into the liquid cell holder followed by the small bottom E-chip.

A solution of the aqueous ZnS sample (0.5 μL) was then dispensed onto the window of the bottom E-chip while carefully holding the chip in place with tweezers to prevent the small chip from adhering to the end of the micropipette tip. The large top chip was placed on top of the bottom E-chip when the solution was nearly dry (i.e., with only a small amount of visible water layer remaining on the small chip). This drying process was performed to attain the thinnest aqueous layer to maximize the imaging resolution in STEM mode. The large top chip was then checked to ensure that the bottom chip and top chip windows were well aligned relative to each other and also in the holder. Once properly seated the top clamp of the holder was placed and the chips were rechecked to ensure proper seating. The liquid cell was then secured with three screws to hermetically seal the system (SI Fig. S1 and Fig.S2). A Hummingbird leak check station was used with an adapter for the HF-3300 holder to test the quality of the seal in the liquid cell system. The tubing ports were left open to air and pumped down to about 6×10^{-6} mbar ($\sim 4.5 \times 10^{-6}$ torr) prior to inserting the liquid cell holder into the TEM to ensure a hermetic seal. The beam current at the sample was checked using the Faraday cup on a Gatan double tilt holder.

Single particle and total area (video frame) dissolution curves were extracted from the dark field (DF) images using ImageJ software.[45] The DF frames were chosen owing to the difficulty of extracting particle areas in bright field (BF) images due to changes in intensities caused by diffraction contrast and regions of overlapping particles. Each frame in the stack was processed with bright outliers under 2 pixels and the threshold of 50 removed. A mean filter with a 2 pixel radius was then applied to assist in the thresholding for particle analysis. The global thresholding was adjusted to minimize the inclusion of background noise in the total area extraction. This was crucial for the last few frames, in which most of the nanoparticles were dissolved. Individual particle areas were extracted from the threshold images by selecting a region that included the nanoparticle of interest with any additional particles touching the edge of the selected region. The nanoparticle area was extracted with areas touching the edges and areas smaller than 20 pixels^2 excluded. This allowed the extraction of only the nanoparticle region of interest with all neighboring particles and background noise excluded. Similarly, total area extraction was performed on the threshold images using the particle analysis component with edges included and areas smaller than 20 pixels^2 excluded. Examples of the single particle and total area data extractions are shown in SI Fig. S3 and S4.

Dissolution Rate Calculation: The change in radius as a function of time for an isolated ZnS nanoparticle (assuming a spherical particle) was fit by using a modified form of the Kelvin equation [Eq. (1)] as discussed by Jiang et al.[37]

$$\frac{d(r)}{dt} = ae^{\frac{r_c}{r}} \quad (1)$$

$$r_t = r_{t-\Delta t} - ae^{\frac{r_{Crit}}{r_{t-\Delta t}}} \quad (2)$$

$$a = \frac{KS_0}{\rho} \quad (3)$$

where r_t is the nanoparticle radius at some time point t, r_0 is the initial nanoparticle radius, Δt is a small change in time and in this case is the frame rate (2 s/frame), K is a constant related to the dissolution environment, S_0 is the bulk solubility of the ZnS phase, and ρ is the density of the bulk ZnS phase. Images were collected at the same magnification to maintain a relatively constant dissolution environment. The critical radius, r_c, at which the nanoparticle is stable is related to the surface energy of the particle by the modified Kelvin equation:[37]

$$r_c = \frac{2\gamma V_m N_A}{10^{18} RT} \quad (4)$$

where γ is the surface free energy of the nanoparticle in J/m^2, V_m is the molecular volume of the ZnS phase of the nanoparticle, N_A is Avogadro's number, 10^{18} is a conversion factor for the surface energy to J/nm^2, R is the ideal gas constant, and T is the temperature in Kelvin. V_m for the sphalerite form of ZnS is 0.03939 nm^3/molecule.[46] The data was nonlinear least squares fit to the equations above using a Levenberg–Marquardt algorithm in MathCAD. Single nanoparticle dissolution curves for each sample type were fit simultaneously with a and r_c being fit globally, while the r_0 values for each curve were fit individually.

After obtaining the r_c values for each sample, Eq. (4) was rearranged to Eq. (5) and used to solve for the apparent surface free energy (γ).

$$\gamma = \frac{10^{18} r_c RT}{2 V_m N_A} \quad (5)$$

RESULTS AND DISCUSSION

Particle Size and Chemical Characterization. The transmission electron micrographs reveal a tendency for all the ZnS samples to aggregate after being deposited onto TEM grids. The abio-ZnS1, bio-ZnS1, and bio-ZnS2 samples displayed a similar pattern under the microscope, that is, a loose, disordered packing arrangement after being deposited onto the grid (Fig. 1). The average

particle size based on TEM measurements was estimated to be 4.57 ± 1.0 nm for abio-ZnS1 (n = 210), 8.22 ± 2.88 nm for bio-ZnS1 (n = 206), and 3.17 ± 1.09 nm for bio-ZnS2 (n = 220). Conversely, the abio-ZnS2 sample, which was produced by bubbling H_2S gas, resulted in large aggregates that consisted of smaller particles with an average size of 2.87 ± 0.74 nm (n = 200). These results illustrate that the bio-ZnS1 sample contained the largest individual nanoparticles; the sizes of the individual nanoparticles present in abio-ZnS1, abio-ZnS2, and bio-ZnS2 were statistically the same. This is similar to the observations of others, who observed that the largest nanoparticles resulted from biogenic processes.[4]

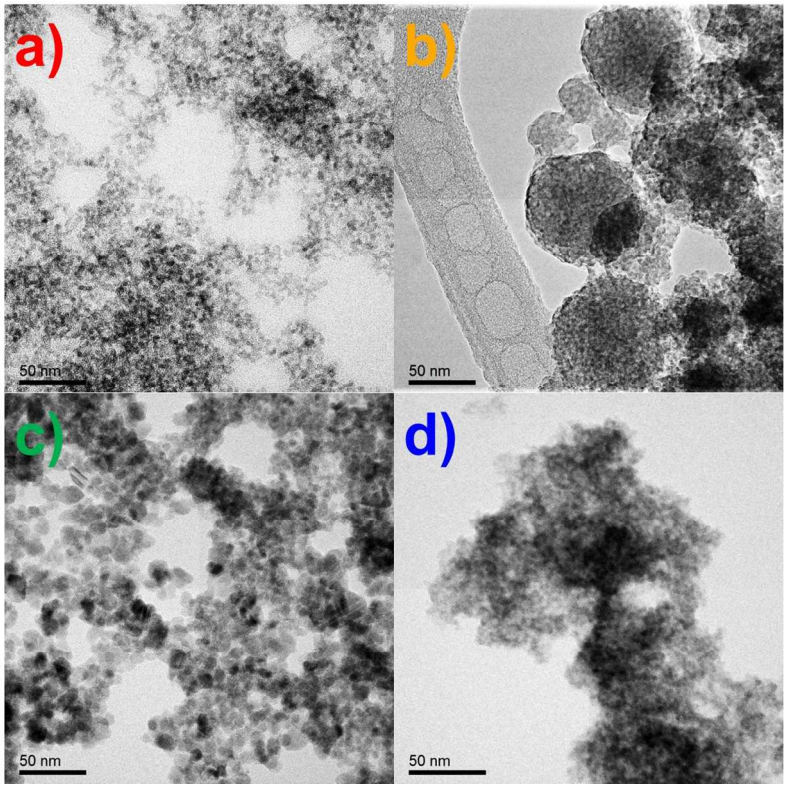

Fig. 1. TEM images of the four ZnS samples. a) abio-ZnS1, produced abiotically with zinc chloride and sodium sulfide; b) abio-ZnS2, produced abiotically with zinc acetate and biologically produced H_2S gas; c) bio-ZnS1, produced biologically with *Thermoanaerobacter* sp. X513; d) bio-ZnS2, produced biologically with *Thermoanaerobacter* sp. X513 with added Ag.

X-ray EDS maps confirm the presence of Zn and S in all the abiogenic and biogenic samples (Fig. S5). The results also showed that the abio-ZnS2, bio-ZnS1, and bio-ZnS2 contained carbon in the ZnS aggregates, whereas the abio-ZnS1 had relatively little. The stronger carbon peaks are likely the result of capping agents, more specifically acetate in the abio-ZnS2 sample and organic compounds from microbial metabolites in the bio-ZnS1 and bio-ZnS2 samples. All of the samples, especially the aggregated areas demonstrated the presence of oxygen in the EDS analysis with the abio-ZnS2 sample being the most prominent. The oxygen peak is likely due to adsorbed water molecules since these samples were not dried at elevated temperatures prior to imaging.

High-Resolution Transmission Electron Microscopy and Structural Characterization. The crystal structure of the ZnS samples were analyzed using Fast Fourier Transform (FFT) of HRTEM images and SAED patterns, and were determined to be predominantly sphalerite (zinc blend) (Fig. S6 and S7). The calculated d-spacing for the dominant faces, based on the SAED patterns of the samples, are compared to sphalerite reference patterns in Table 1, showing high consistency.

Table 1. Selected area electron diffraction results for the ZnS samples along with literature values for sphalerite[47]

Sample	Lattice spacings (Å)		
	Miller index		
	111	220	311
abio-ZnS1	3.14	1.92	1.64
abio-ZnS2	3.05	1.87	1.63
bio-ZnS1	3.14	1.91	1.64
bio-ZnS2	3.09	1.88	1.63
sphalerite[47]	3.1231	1.9125	1.631

Beam damage was observed in select sample locations where the electron beam was focused for extended periods of time. This is evident by the transformation of ZnS to ZnO as observed by the additional reflections in the FFT of the HRTEM image for abio-ZnS2 (Fig. 2b).[48, 49]

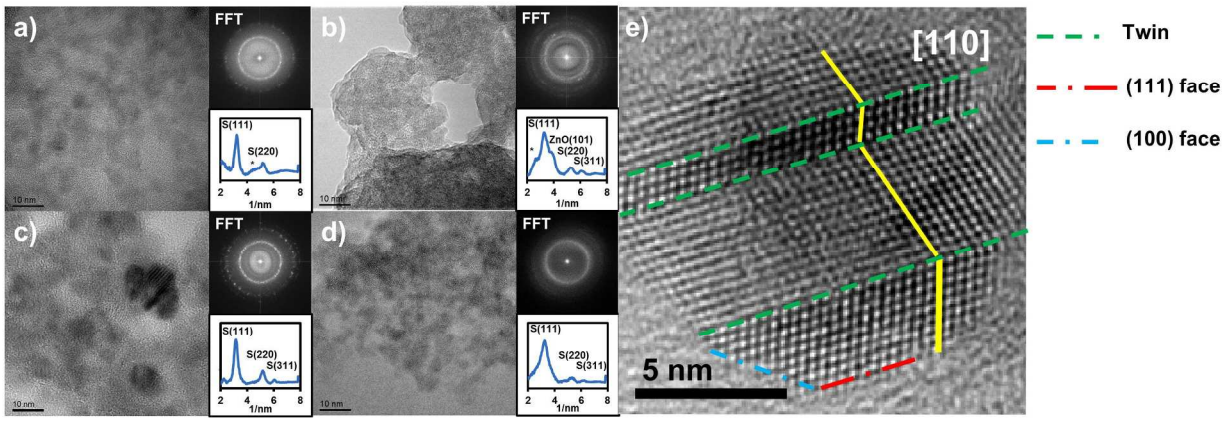

Fig. 2. HRTEM images of the ZnS nanoparticles with corresponding fast-Fourier transforms of the HRTEM images and corresponding background-subtracted radial distance profiles. Sphalerite (S) and zincite (ZnO) peaks are assigned. a) abio-ZnS1, b) abio-ZnS2, c) bio-ZnS1, d) bio-ZnS2. HRTEM image of the bio-ZnS1 sample viewed down the {110} zone axis, showing multiple twins along the {111} faces and nanoparticle surface faces (e).

Influence of Aqueous Conditions on Formation and Growth Mechanisms. As previously mentioned, the aqueous condition during nanoparticle formation can influence OA, thereby controlling the surface reactivity of nanoparticles and thus individual nanoparticles' size and shape.[31, 32] We evaluated this by synthesizing nanoparticles in solutions with agents that either promoted, inhibited, or had relatively little influence on the OA of the nanoparticles. In the case of bio-ZnS1, multiple defects were observed in TEM images (i.e., stacking faults, dislocations, and twinning), which are likely the result of biogenic polymers serving to promote OA (Fig. 2e).

The occurrence of structural defects in the biogenic nanocrystals is likely an intrinsic feature of ZnS crystallites formed in low-temperature aqueous solutions, and these defects become more apparent with increasing crystallite size. As discussed in several previous studies,[4, 18] the dipole–dipole interactions between ZnS nuclei formed in low-temperature aqueous environments and water molecules can cause significant structural strains. Although previous computational results (e.g., those in Spano et al., [50]) suggest that such strains could modify nanosized ZnS from sphalerite-like structures to bubble-like polyhedral structures, to the best of our knowledge the latter ones have never been reported in experimental work. Instead, stacking disorders frequently have been observed in nanocrystals of metal chalcogenides.[51, 52] Therefore, the water-induced structural strains in the ZnS nanostructures are more likely released on account of variations in the stacking orders of the {111} faces (e.g., stacking faults) rather than relaxing the overall nanoparticle structure. Therefore, the stacking faults observed in the bio-ZnS1 samples are a combination of OA- and water-induced structural strain, with OA probably being the dominant mechanism contributing to the defect sites.

Formation of the bio-ZnS1 sample likely occurs though the OA promotion interactions. In the absence of Ag, organic media components and bacterial by-products play the dominant role in the formation of the multiple defects observed in the larger nanoparticles by mediating the OA process. Organic molecules and proteins from microbial activity (e.g., aliphatics [lipids] and amines) were identified in these samples (see FTIR spectra in SI Fig. S8). The twinning in the bio-ZnS1 samples was observed along the {111} faces of the crystals and is consistent with twinning observed by Xu et al.[4] and Huang et al.[53]. Multiple defects, such as twinning, were also observed in individual particles. The twinning leads to the formation of {111} and {100} faces on the outside of the nanoparticles (Fig. 2e). Twinning or stacking faults in the bio-ZnS1 sample

were observed in about 1% of all the nanoparticles, yet this is an underestimate because nanocrystals were aligned out of the zone axis required to observe twinning along these boundaries. Twinning at the polar {111} faces may have been facilitated by the stabilization of the nonpolar {110} faces through the binding of nonpolar organic molecules such as aliphatics (lipids), leaving the {111} faces exposed to react with neighboring particles through OA mechanisms.

We did not observe a significant fraction of defects in the other three samples (abio-ZnS1, abio-ZnS2, and bio-ZnS2), which were synthesized either in the presence of an inhibitor (e.g., acetate or Ag) or in neutral solutions (devoid of either an inhibitors or promoters).

The composition of the abio-ZnS2 and bio-ZnS2 solutions appears to inhibit OA, resulting in smaller nanoparticles that lack defects (i.e., twins and stacking faults). Although both inhibit the formation of defects, the way it occurs differs between acetate and Ag. The inhibition of abio-ZnS2 OA is influenced by the presence of acetate in the solution. Acetate is known to stabilize quantum-dot-sized nanoparticles, and acetate is present on the surface of these particles (see FTIR spectra for abio-ZnS2 in SI Fig. S8).[54] Although a known stabilizer, acetate around metals is easily displaced by sulfides upon exposure to H_2S gas.[55] Because acetate is a polar molecule and the ZnS sphalerite phase can form polar faces,[23, 56] we propose here that binding of acetate to ZnS nanoparticles favors the polar faces (i.e., {111} and {100}), thus stabilizing these high-surface-energy faces and leaving the lower-surface-energy nonpolar faces exposed. Interactions of these non-polar faces led to flocculation of the ZnS nanoparticles (Fig. 1). Similar effects were observed for thioglycerol-capped ZnS nanoparticles formed in ethanol and water solutions at 60 °C.[57] Thus, the polarity of the capping agent in solution plays a significant role in particle aggregation.

Unlike bio-ZnS1, the bio-ZnS2 sample was synthesized in the presence of Ag ions, and the resulting ZnS nanoparticles lack defects. However, we cannot fully explain the reason for the lack of defects in the bio-ZnS2 sample. One plausible explanation is the difference in aqueous reaction free energies between Zn and Ag, which may result in localized nucleation of Ag_2S along the edges of abio-ZnS2 crystals and thus limit OA.[58] Although plausible, we did not positively identify Ag in EDS maps of the bio-ZnS2 sample likely because of the low concentration of Ag (1:10 Ag to Zn).

A few crystallites ~4 nm in size in the abio-ZnS1 sample were observed to have defects, specifically single twin boundaries, which could be the result of water-induced structural strain. Under the neutral solution synthesis conditions, OA appear to be minimal, suggesting nucleation as the driver for growth rather than OA.

In Situ ZnS Nanoparticle Dissolution. LCTEM was used to conduct in situ dissolution experiments on each ZnS nanoparticle sample to evaluate the influence of the presence of defects on the dissolution behavior of ZnS nanoparticles. All LCTEM measurements were performed in scanning TEM (STEM) mode. Here we focus our discussion on bio-ZnS1 and abio-ZnS1, which represent ZnS nanoparticles with and without defects, respectively. The abio-ZnS2 and bio-ZnS2 samples were excluded from these measurements because of the particle size, the confounding effects of Ag (bio-ZnS2), and the tightly packed aggregates that made it difficult to avoid near-neighbor interactions. Individual ZnS nanoparticles can be clearly seen in simultaneously captured BF and DF STEM images for bio-ZnS1 (SI Fig. S9).

In addition to clearly observing distinct nanoparticles, we find that changes in beam dose (e.g., magnification changes) can influence nanoparticle dissolution (Supporting Information video). This is consistent with the theoretical calculations of Schneider et al.[38], which demonstrate that

higher beam doses can increase the types and amounts of reactive electrolysis byproducts, such as the formation of pH-lowering hydronium ions [Eq. (6)]. Based on Schneider's heterogeneous model predictions,[38] the electron-beam-induced reactions, such as pH changes and formation of solvated electrons, occur only in the localized area of the electron beam during imaging, and the reactions achieve steady state in milliseconds.[38, 59] Here we assume that the localized pH effect represents the driving force for the dissolution of the ZnS nanoparticles. An example demonstrating that the beam effects are localized is displayed in SI Fig. S10.

$$ZnS + 2H^+ \rightarrow Zn^{2+} + H_2S \quad (6)$$

Computationally calculated surface energies for the sphalerite form of ZnS range from 0.38 to 2.56 J/m^2 depending on the crystal face with reported total average surface free energies ranging from 0.79 to 1.00 J/m^2.[23,60] In all cases the lowest energy crystal face is the {110} face with mean values ranging from 0.39 to 0.65 J/m^2. Other predominant crystal faces, such as the {111} and {100} faces, have values ranging from 0.87 to 1.84 J/m^2 and 1.21 to 2.56 J/m^2 respectively.[60] Experimentally measured surface energies of ZnS nanoparticles have ranged from 0.50 to 0.58 J/m^2.[61]

Individual nanoparticle dissolution curves of the bio-ZnS1 and abio-ZnS1 samples and their corresponding fitted curves are shown in Fig. 3. The corresponding a, r_c, r_0, and calculated γ values for each sample type are shown in **Table 2**. Overall, the calculated surface energies of the ZnS samples are within reasonable value ranges compared to the previously reported ones.[23, 61] The bio-ZnS1 sample has the highest surface energy, while the abio-ZnS1 sample has the lowest average surface energy.

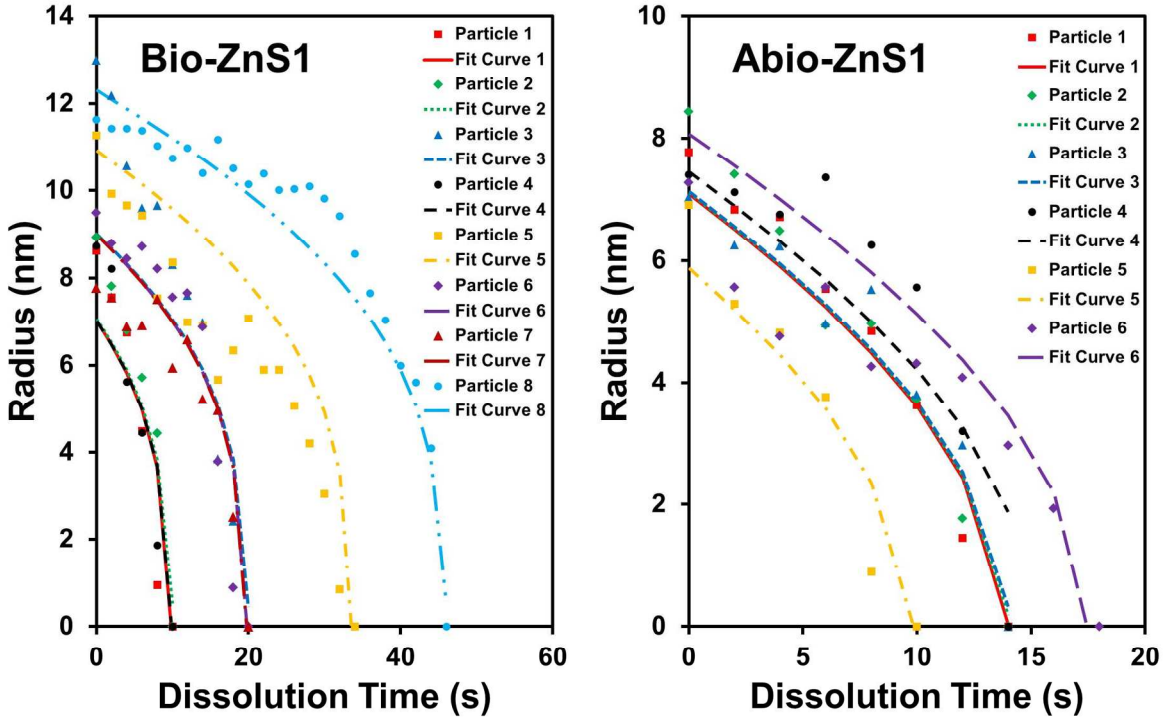

386

387 **Fig. 3.** Nonlinear least squares fit of individual ZnS nanoparticles dissolution for the bio-ZnS1 and abio-ZnS1

388 samples.

389

390 **Table 2.** Nonlinear least squares fit values for the dissolution of different bio-ZnS1 and abio-ZnS1 samples

Parameters	bio-ZnS1	abio-ZnS1
a	0.061	0.272
r_c (nm)	15.3	5.298
r_0 (nm)	7.016, 7.065, 9.019, 7.022, 10.92, 8.99, 8.987, 12.312	7.09, 7.109, 7.127, 7.451, 5.875, 8.073
γ (J/m^2)	0.799	0.277
Average NRMSE%	14.92	11.68

391

392 Previous work on ZnS nanoparticle dissolution in EDTA attributed the lower surface free

393 energy (0.50 J/m^2) relative to the average surface free energy (0.86 J/m^2) to the hydration and

394 hydroxylation of ZnS nanoparticle surfaces, yet the impacts of specific crystal faces on the

measured surface energies are not discussed.[61] Hamad's calculations predict that the most stable morphology (i.e., a set of faces enclosing a particle) of the sphalerite form of ZnS is completely enclosed by the {110} set of faces.[23] As mentioned above the calculated surface energies for the {110} faces range from 0.39 to 0.65 J/m^2.[23, 60] Thus, it is possible that the lower surface energies of the abio-ZnS1 samples in this work, as well as those observed by Zhang et al. [23], are a result of small nanoparticles bounded by predominantly {110} faces resulting in the lower measured surface free energies.

This brings into question why does the bio-ZnS1 samples have a higher surface free energy (0.80 J/m^2). As discussed above the bio-ZnS1 sample has many defects consisting of twin boundaries predominantly on the {111} sets of faces as well as stacking faults when viewed down the [110] zone axis. The effect of this twinning along the {111} faces results in more of the {111} and {100} crystal faces on the outside of the nanoparticle. These faces are seen as the edges of the 2D projection of the 3D nanocrystal as shown in Fig. 2e by the blue and red lines. Since the measured areas are a result of this projection, the observed dissolution behavior is related to the specific crystal faces observed by this projection onto the detector. Closer examination of the bio-ZnS1 dissolution images reveals what appear to be two types of nanoparticles, round faceted and rod-like particles (red circles and green triangles in Fig. 4, respectively). During the dissolution, some of the rod-like structures are observed to rotate down to reveal a structure resembling the round faceted particles, illustrating that a single type of nanoparticle is present in bio-ZnS1 (Fig. S11). In the cases where the rod-like structures do not rotate downward, the dissolution direction is faster in the long axis. This behavior results in an anisotropic dissolution of the crystal (Fig. 4 green triangles). Considering the significant number of defects observed in the HRTEM images of this sample and the fact that the lower energy faces

418 dissolve more slowly, based on Eqs. (1) and (3), the slowest dissolving face is likely the {110}
419 face, while the faster dissolving faces are the {111} and {100} faces. The {110} face is
420 perpendicular to the {111} and {100} faces. The presence of these more reactive faces in the
421 higher-defect-containing bio-ZnS1 sample has led to the higher surface energies observed for
422 this sample and is in good agreement with calculated energies for the {111} faces of the
423 sphalerite form of ZnS.[23, 60]
424

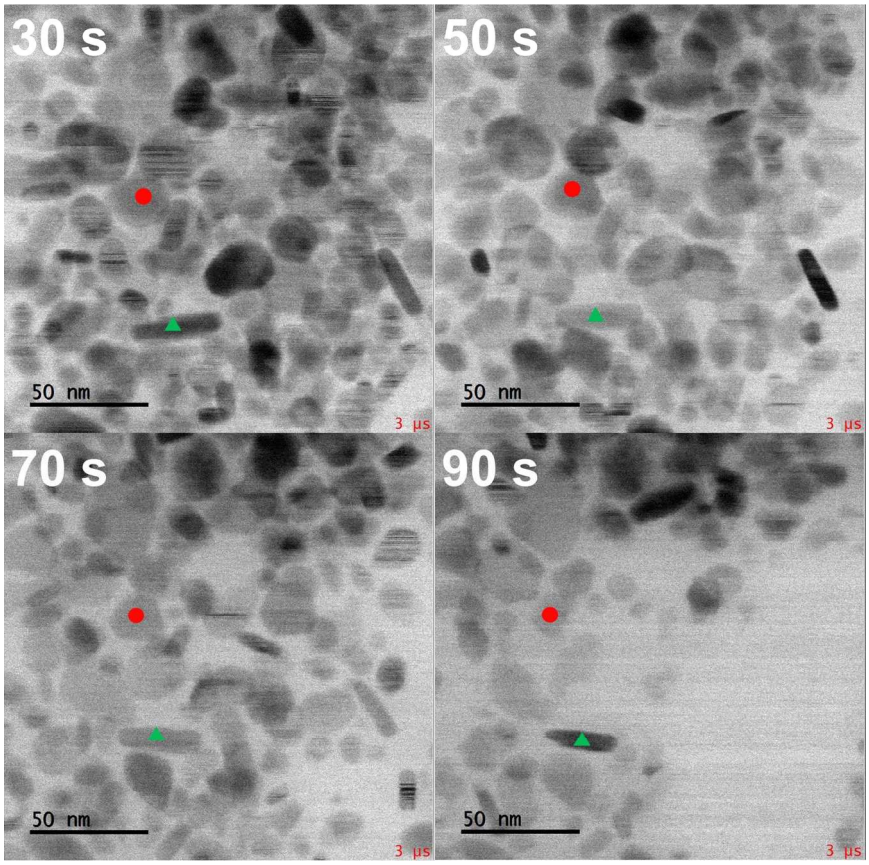

425
426 **Fig. 4.** Time-dependent still frames of the bio-ZnS1 nanoparticle dissolution, showing the preferred dissolution of
427 specific faces in the liquid cell. Anisotropic dissolution is observed in the last stages for both the round faceted (red
428 circles) and the rodlike (green triangles) particles.
429

Some previous studies suggested that dissolution occurs more rapidly at defect locations.[4] Even with the maximum resolution selected for our liquid cell images, we were unable to clearly observe dissolution along the twin boundaries in the bio-ZnS1 sample. However, specific faces were observed to retreat inward faster than others, but without higher resolution LCTEM images, we cannot definitively determine if the defect sites control the observed dissolution retreat.

For estimating the total area dissolution in the LCTEM images, a single frame was modeled using the calculated a and r_c values (**Table 2**). The initial nanoparticle radii were measured in the first frame using the BF images and entered as the starting r_0 values. The sum of the areas was then calculated as each of the nanoparticles dissolved in the simulation. The total calculated area was minimized to best fit the data with a multiplying factor, α, to account for an overestimate in the total area due to particle–particle overlap and the differences in the area between the BF and DF images. This method generated an accurate prediction for regions of the sample with well-separated nanoparticles (Fig. 5a). In image locations with nanoparticles in close proximity to one another, the agreement between measured and calculated is poor (Fig. 5b). Other researchers have observed similar behavior and suggest that neighboring nanoparticles can slow the dissolution of other nanoparticles when space between them is tight.[37] This close packing effect explains the poor agreement between measured and calculated dissolution. In order to further explore the impact of particle packing on dissolution, we consider the possibility that adjacent nanoparticles in the tightly packed image may dissolve as a single unit. The results of this analysis is shown in Fig. 5b and illustrate that if we assume the radius is two times the size of the individual particles, we are able to capture the phenomenon. Future studies are needed to better explain the impact of neighboring nanoparticles on the estimate of total area dissolution rate.

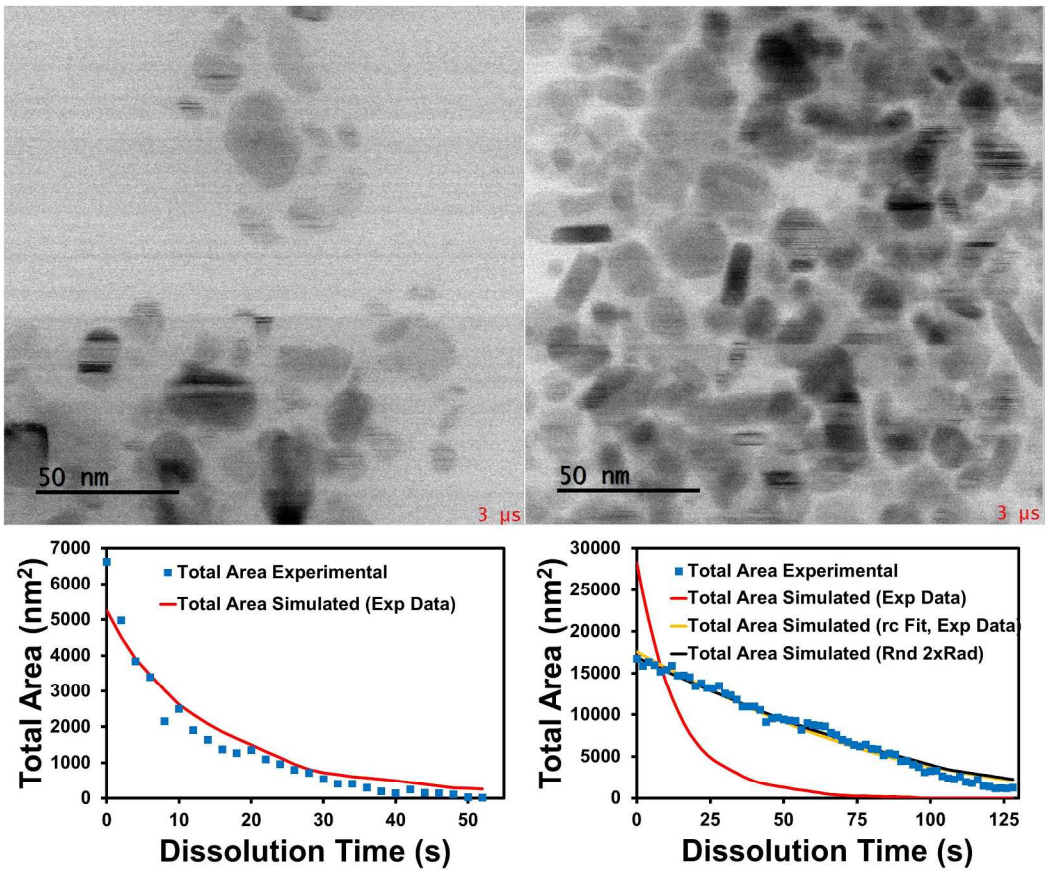

452

453 **Fig. 5.** First frames of the bio-ZnS1 nanoparticle solution in a) well dispersed and b) aggregated areas of the sample.

454 The corresponding total measured areas and simulated data are shown for each dissolution video.

455

456

457 **Table 3.** Parameters used for total area dissolution for bio-ZnS1 sample

	Avg. Particle Radius	Standard. Deviation	□□	α	NRMSE	N
Exp. (a)	7.1	2.9	15.3	0.517	6.2	55
Exp. (b)	7.5	2.6	15.3	0.896	39.912	160
Exp. (b), r_c Fit	7.5	2.6	2.96	0.558	4.361	160
Exp. (b), 2 × radius	15.5	5.3	15.3	0.251	1.137	80

Avg. Particle Radius – average radius for particles in image.
Std. Dev. – standard deviation of the radius for particles in image.
N – number of particles.
α – multiplying factor.
NRMES – normalized root mean squared error.
Exp. (a) – Experiment (a) for well dispersed particles.
Exp. (b) – Experiment (b) for aggregated area of sample.
Exp. (b), r_c Fit – Experiment (b) refined r_c for aggregated area of sample using experimental radii.
Exp. (b), 2 × radius – Experiment (b) two times the particle radius for aggregated area of sample.

458

459 This study demonstrates that LCTEM is a viable technique for evaluating the dynamics of ZnS
460 nanoparticle stability. Furthermore, the results show that biogenic ZnS nanoparticles with defects
461 are more reactive than smaller quantum-dot-sized nanoparticles, and that the formation
462 conditions, which include the presence of other trace elements and organic molecules, can have a
463 significant impact on ZnS nanoparticle size and ultimately dissolution behavior. Last, these
464 results provide new insight into the factors that govern the formation, aggregation, and stability
465 of biogenic ZnS nanoparticles in environmental systems, and thus have broader implications for
466 predicting the bioavailability and fate of Zn, Cd, and Hg in water-sediment systems, especially at
467 transition zones or interfaces where steep changes in microbial community, water chemistry, and
468 redox conditions occur.

469

470

ASSOCIATED CONTENT

Supporting Information

The Supporting Information is available free of charge on the ACS Publications website.

Provided in the Supporting Information are details of materials synthesis and microscopy sample preparation and imaging, additional details on liquid-cell TEM, examples of image analysis, supplemental STEM and TEM information, example dissolution videos for the abio-ZnS1 and bio-ZnS1, and data for the single particle fits.

AUTHOR INFORMATION

***Corresponding Author: pierceem@ornl.gov, Phone: (865) 574-9968, Fax: (865) 576-8646**

Author Contributions: EMP conceived and organized the research study; **JWM and JRE** synthesized the samples tested; **JRE**, **JX**, **MC**, and **EMP** collected, analyzed, and interpreted the microscopy data; and **JRE**, **JX**, **DG**, **JWM**, **BG**, and **EMP** contributed to the manuscript. All authors have given approval to the final version of the manuscript.

ACKNOWLEDGMENT

This research was sponsored by the Office of Biological and Environmental Research (BER), Office of Science, US Department of Energy (DOE) as part of the Mercury Science Focus Area at Oak Ridge National Laboratory (ORNL), which is managed by UT-Battelle LLC for DOE under contract DE-AC05-00OR22725. The nanoparticle biosynthesis was sponsored in part by the DOE Advanced Manufacturing Office, Low Temperature Material Synthesis Program (CPS 24762).

The authors declare no competing financial interest.

REFERENCES

1. Hochella, M. F.; Lower, S. K.; Maurice, P. A.; Penn, R. L.; Sahai, N.; Sparks, D. L.; Twining, B. S., Nanominerals, mineral nanoparticles, and Earth systems. *Science* **2008,** *319*, 1631-1635.
2. Hochella, M. F.; Aruguete, D. M.; Kim, B.; Madden, A. S., Naturally occurring inoragnic nanoparticles: General assessment and a global budget for one of Earth's last unexplored geochemical components. In *Nature's Nanostructures*, Guo, H.; Barnard, A., Eds. Pan Stanford Publishing: Victoria, Australia, 2012.
3. Hochella, M. F.; Moore, J. N.; Putnis, C. V.; Putnis, A.; Kasama, T.; Eberl, D. D., Direct observation of heavy metal-mineral association from the Clark Fork River Superfund Complex: implications for metal transport and bioavailability. *Geochimica et Cosmochimica Acta* **2005,** *69*, 1651-1663.
4. Xu, J.; Murayama, M.; Roco, C. M.; Veeramani, H.; Michel, F. M.; Rimstidt, J. D.; Winkler, C.; Hochella, M. F., Highly-defective nanocrystals of ZnS formed via dissimilatory bacterial sulfate reduction: A comparative study with their abiogenic analogues. *Geochimica et Cosmochimica Acta* **2016,** *180*, 1-14.
5. Moreau, J. W.; Webb, R. I.; Banfield, J. F., Ultrastructure, aggregation-state, and crystal growth of biogenic nanocrystalline sphalerite and wurtzite. *American Mineralogist* **2004,** *89*, 950-960.
6. Moreau, J. W.; Weber, P. K.; Martin, M. C.; Gilbert, B.; Hutcheon, I. D.; Banfield, J. F., Extracellular proteins limit the dispersal of biogeonic nanoparticles. *Science* **2007,** *316*, 1600-1603.
7. Labrenz, M.; Druschel, G.; Thomsen-Ebert, T.; Gilbert, B.; Welch, S. A.; Kemner, K. M.; Logan, G. A.; Summons, R. E.; De Stasio, G.; Bond, P. L.; Lia, B.; Kelly, S.; Banfield, J. F., Formation of sphalerite (ZnS) deposits in natural biofilms of sulfate-reducing bacteria. *Science* **2000,** *290*, 1744-1747.
8. Hsu-Kim, H.; Mullaugh, K. M.; Tsang, J. J.; Yucel, M.; Luther III, G. W., Formation of Zn- and Fe-sulfides near hydrothermal vents at the Eastern Lau Spreading Center: implications for sulfide bioavailability to chemoautotrophs. *Geochemical Transactions* **2008,** *9*, (6), 1-14.
9. Luther III, G. W.; Rozan, T. F.; Taillerfert, M.; Nuzzio, D. B.; Di Meo, C.; Shank, T. M.; Lutz, R. A.; Cary, S. C., Chemical speciation drives hydrothermal vent ecology. *Nature* **2001,** *410*, 813-816.
10. Trudinger, P. A.; Chambers, L. A.; Smith, J. W., Low-temperature sulphate reduction: biological vs. abiological. *Canadian Journal of Earth Science* **1985,** *22*, 1910-1918.
11. Liu, J.; Aruguete, D. M.; Jinschek, J. R.; Rimstidt, J. D.; Hochella, M. F., The non-oxidative dissolution of galena nanocrystals: insights into mineral dissolution rates as a function of grain size, shape, and aggregation state. *Geochimica et Cosmochimica Acta* **2008,** *72*, 5984-5996.
12. Gondikas, A. P.; Jang, E. K.; Hsu-Kim, H., Influence of amino acids cysteine and serine on aggregation kinetics of zinc and mercury sulfide colloids. *Journal of Colloid and Interface Science* **2010,** *347*, 167-171.
13. Gondikas, A. P.; Mason, A.; Auffan, M.; Lau, B. L. T.; Hsu-Kim, H., Early-stage precipitation kinetics of zinc sulfide nanoclusters forming in the presence of cysteine. *Chemical Geology* **2012,** *329*, 10-17.

14. Rozan, T. F.; Lassman, M. E.; Ridge, D. P.; Luther III, G. W., Evidence of iron, copper, and zinc complexation as multinuclear sulphide clusters in oxic rivers. *Nature* **2003,** *406*, 879-882.
15. Theberge, S. M.; Luther III, G. W.; Farrenkopf, A. M., On the existence of free and metal complexed sulfide in the Arabian Sea and its oxygen minimum zone. *Deep-Sea Research* **1997,** *44*, 1381-1390.
16. Priadi, C.; Le Pape, P.; Morin, G.; Ayrault, S.; Maillot, F.; Juillot, F.; Hochreutener, R.; Llorens, I.; Testemale, D.; Proux, O.; Brown, G. E., X-ray absorption fine structure evidence for amorphous zinc sulfide as a major zinc species in suspended matter from the Seine River downstream of Paris, Ile-de-France. *Environmental Science and Technology* **2012,** *46*, 3712-3720.
17. Zhang, H.; Banfield, J. F., Energy Calculations Predict Nanoparticle Attachment Orientations and Asymmetric Crystal Formation. *Journal of Physical Chemistry Leters* **2012,** *3*, (19), 2882-2886.
18. Gilbert, B.; Banfield, J. F., Molecular-scale processes involving nanoparticulate minerals in biogeochemical systems. In *Molecular Geomicrobiology*, Banfield, J. F.; Cervini-Silva, J.; Nealson, K. H., Eds. Mineralogical Society of America and Geochemical Society: 2005; pp 109-156.
19. Kortan, A. R.; Hull, R.; Opila, R. L.; Bawendi, M. G.; Steigerwald, M. L.; Carroll, P. J.; Brus, L. E., Nucleation and growth of CdSe and ZnS quantum crystallite seeds, and vice versa, in inverse micelle media. *Journal of American Chemical Society* **1990,** *112*, 1327-1332.
20. Daskalakis, K. D. a. H., G.R., The solubility of sphalerite (ZnS) in sulfidic solutions at 25 °C and 1 atm pressure. *Geochimica et Cosmochimica Acta* **1993,** *57*, 4923-4931.
21. Helz, G. R.; Charnock, J. M.; Vaughan, D. J.; Garner, C. D., Multinuclearity of aqueous copper and zinc bisulfide complexes: an EXAFS investigation. *Geochimica et Cosmochimica Acta* **1993,** *54*, 15-25.
22. Luther III, G. W.; Theberge, S. M.; Rickard, D. T., Evidence for aqueous clusters as intermediates during zinc sulfide formation. *Geochimica et Cosmochimica Acta* **1999,** *63*, 3159-3169.
23. Hamad, S.; Cristol, S.; Catlow, C. R. A., Surface Structures and Crystal Morphology of ZnS: Computational Study. *The Journal of Physical Chemistry B* **2002,** *106*, (42), 11002-11008.
24. Shea, D.; MacCrehan, W. A., Role of biogenic thiols in the solubility of sulfide minerals. *Science of the Total Environment* **1988,** *73*, 135-141.
25. Vairavamurthy, A.; Mopper, K., Field methods for determination of traces of thiols in natural water. *Analytica Chimica Acta* **1990,** *236*, 363-370.
26. Zhang, J.; Wang, F., Thiols in wetland interstitial waters and their role in mercury and methylmercury speciation. *Limnology and Oceanography* **2004,** *49*, (6), 2276-2286.
27. Teng, H., How Ions and Molecules Organize to Form Crystals. *Elements* 2013, pp 189-194.
28. Vreeland, E.; Watt, J.; Schober, G.; Hance, B.; Austin, M.; Price, A.; Fellows, B.; Monson, T.; Hudak, N.; Maldonado-Camargo, L.; Bohorquez, A.; Rinaldi, C.; Huber, D., Enhanced Nanoparticle Size Control by Extending LaMer's Mechanism. *Chemistry of Materials* **2015,** *27*, 6059-6066.
29. Burton, W.; Cabrera, N.; Frank, F., The growth of crystals and the equilibrium structure of their surfaces. *Royal Society of London Philosophical Transactions A* **1951,** *243*, 299-358.

30. De Yoreo, J. J.; Gilber, P. U. P. A.; Sommerdijk, N. A. J. M.; Penn, R. L.; Whitelam, S.; Joester, D.; Zhang, H.; Rimer, J. D.; Navrotsky, A.; Banfield, J. F.; Wallace, A. F.; Michel, F. M.; Meldrum, F. C.; Colfen, H.; Dove, P. M., Crystallization by particle attachment in syntetic, biogenic, and geologic environments. *Science* **2015,** *349*, (6247), aaa6760-1-9.
31. Zhang, J.; Lin, Z.; Lan, Y.; Ren, G.; Chen, D.; Huang, F.; Hong, M., A Multistep Oriented Attachment Kinetics: Coarsening of ZnS Nanoparticle in Concentrated NaOH. *Journal of the American Chemical Society* **2006,** *128*, (39), 12981-12987.
32. Langille, M. R.; Personick, M. L.; Zhang, J.; Mirkin, C. A., Defining Rules for the Shape Evolution of Gold Nanoparticles. *Journal of the American Chemical Society* **2012,** *134*, (35), 14542-14554.
33. Ye, X.; Jin, L.; Caglayan, H.; Chen, J.; Xing, G.; Zheng, C.; Doan-Nguyen, V.; Kang, Y.; Engheta, N.; Kagan, C. R.; Murray, C. B., Improved Size-Tunable Synthesis of Monodisperse Gold Nanorods through the Use of Aromatic Additives. *ACS Nano* **2012,** *6*, (3), 2804-2817.
34. Hufschmid, R.; Newcomb, C.; Grate, J.; De Yoreo, J. J.; Browning, N.; Qafoku, N., Direct visualization of aggregate morphology and dynamics in a model soil organic-mineral system. *Environmental Science and Technology Letters* **2017,** *4*, (5), 186-191.
35. Grogan, J. M.; Rotkina, L.; Bau, H. H., In situ Liquid-Cell Electron Microscopy of Colloid Aggregation and Growth Dynamics. *Physical Review E* **2011,** *83*, 061405.
36. Takasaki, M.; Kimura, Y.; Yamazaki, T.; Oaki, Y.; Imai, H., 1D Oriented Attachment of Calcite Nanocrystals: Formation of Single-Crysalline Rods Through Collision. *RSC Advances* **2016,** *6*, 61346-61350.
37. Jiang, Y.; Zhu, G.; Dong, G.; Lin, F.; Zhang, H.; Yuan, J.; Zhang, Z.; Jin, C., Probing the oxidative etching induced dissolution of palladium nanocrystals in solution by liquid cell transmission electron microscopy. *Micron* **2017,** *97*, 22-28.
38. Schneider, N. M.; Norton, M. M.; Mendel, B. J.; Grogan, J. M.; Ross, F. M.; Bau, H. H., Electron–Water Interactions and Implications for Liquid Cell Electron Microscopy. *The Journal of Physical Chemistry C* **2014,** *118*, (38), 22373-22382.
39. Moon, J.; Ivanov, I.; Joshi, P.; Armstrong, B.; Wang, W.; Jung, H.; Rondinone, A.; Jellison, J., G; Meyer III, H.; Jang, G.; Meisner, R.; Duty, C.; Phelps, T., Scalable production of microbially-mediated ZnS nanoparticles and application to functional thin films. *Acta Biomaterialia* **2014,** *10*, (10), 4474-4483.
40. Moon, J.; Phelps, T.; Fitzgerald, C.; Lind, R.; Elkins, J.; Jang, G.; Joshi, P.; Kidder, M.; Armstrong, B.; Watkins, T.; Ivanov, I.; Graham, D., Manufacturing demonstration of microbially mediated zinc sulfide nanoparticles in pilot-plant scale reactors. *Applied Microbiology and Biotechnology* **2016,** *100*, (18), 7921-7931.
41. Chatterjee, N.; Bhattacahrjee, B., Hazardous effect of ZnS Nanoparticles on the Feeding Behavior, Growth and Maturation Process of the Asian Striped Catfish, Mystus Vittatus (Bloch, 1794). *International Aquatic Research* **2014,** *6*, 113-125.
42. Becker, W.; Bard, A., Photoluminescence and Photoinduced Oxygen Adsorption of Colloidal Zinc Sulfide Dispersion. *Journal of Physical Chemistry* **1983,** *87*, 4888-4893.
43. Roh, Y.; Liu, S.; Li, G.; Huang, H.; Phelps, T.; Zhou, J., Isolation and characterization of metal-reducing Thermoanaerobacter strains from deep subsurface environments of the Piceance Basin, Colorado. *Applied and Environmental Microbiology* **2002,** *68*, 6013-6020.
44. Jang, G.; Jacobs, C.; Ivanov, I.; Joshi, P.; Meyer III, H.; Kidder, M.; Armstrong, B.; Datskos, P.; Graham, D.; Moon, J., In situ capping for size control of monochalcogenide (ZnS,

CdS and SnS) nanocrystals produced by anaerobic metal-reducing bacteria. *Nanotechnology* **2015,** *26*, (32), 325602.
45. Rasband, W. S. *ImageJ*, U.S. National Institutes of Health: Bethesda, MD, USA, 2007.
46. Hotje, U.; Rose, C.; Binnewies, M., Lattice constants and molar volume in the system ZnS, ZnSe, CdS, CdSe. *Solid State Sciences* **2003,** *5*, (9), 1259-1262.
47. Skinner, B. J., Unit-cell Edges of Natural and Synthetic Sphalerites. *The American Meneralogist* **1961,** *46*, 1399-1411.
48. Loginov, Y. Y.; Kovalev, I. V.; Zelenkov, P. V., The structural defects formation in ZnS under electron irradiation with energy 400 KeV. *IOP Conference Series: Materials Science and Engineering* **2016,** *122*, 012023.
49. Thangaraj, N.; Wessels, B. W., Electron□beam□enhanced oxidation processes in II□VI compound semiconductors observed by high□resolution electron microscopy. *Journal of Applied Physics* **1990,** *67*, (3), 1535-1541.
50. Spano, E.; Hamad, S.; Catlow, C. R. A., Computational Evidence of Bubble ZnS Clusters. *Journal of Physical Chemistry B* **2003,** *107*, 10337-10340.
51. Tolbert, S.; Alivisatos, A. P., Comparison of quantum confinement effects on the electronic absorption spectra of direct and indirect gap semiconductor nanocrystals. *Physical Review Letter* **1994,** *73*, 3266.
52. Tolbert, S.; Alivisatos, A. P., Se EXAFS study of the elevated wurtzite to rock salt structural phase transition in CdSe nanocrystals. In *NATO ASI Proceedings on Nanophase Materials: Synthesis-Properties-Applications*, Hadjipanayis, G.; Siegel, R., Eds. Kluwer Academic Publishers: Dordrecht, 1994; pp 471-482.
53. Huang, F.; Banfield, J. F., Size-Dependent Phase Transformation Kinetics in Nanocrystalline ZnS. *Journal of the American Chemical Society* **2005,** *127*, (12), 4523-4529.
54. Yang, J.; Deivaraj, T. C.; Too, H.-P.; Lee, J. Y., Acetate Stabilization of Metal Nanoparticles and Its Role in the Preparation of Metal Nanoparticles in Ethylene Glycol. *Langmuir* **2004,** *20*, (10), 4241-4245.
55. Clarke, P. H., Hydrogen Sulfide Production by Bacteria. *Journal of General Microbiology* **1953,** *8*, 397-407.
56. Reichardt, C., Solvents and Solvent Effects in Organic Chemistry. In Wiley-VCH Publishers: 2003.
57. Shahid, R.; Toprak, M. S.; Soliman, H. M. A.; Muhammed, M., Low temperature synthesis of cubic phase zinc sulfide quantum dots. *Central European Journal of Chemistry* **2012,** *10*, (1), 54-58.
58. Beberwyck, B. J.; Surendranath, Y.; Alivisatos, A. P., Cation Exchange: A Versatile Tool for Nanomaterials Synthesis. *The Journal of Physical Chemistry C* **2013,** *117*, (39), 19759-19770.
59. Crundwell, F. K., The mechanism of dissolution of minerals in acidic and alkaline solutions: Part III. Application to oxide, hydroxide and sulfide minerals. *Hydrometallurgy* **2014,** *149*, 71-81.
60. Zhang, H.; Huang, F.; Gilbert, B.; Banfield, J. F., Molecular Dynamics Simulations, Thermodynamic Analysis, and Experimental Study of Phase Stability of Zinc Sulfide Nanoparticles. *The Journal of Physical Chemistry B* **2003,** *107*, (47), 13051-13060.
61. Zhang, H.; Chen, B.; Banfield, J. F., Particle Size and pH Effects on Nanoparticle Dissolution. *The Journal of Physical Chemistry C* **2010,** *114*, (35), 14876-14884.

671

672 **List of Figures:**

687

688

List of Tables:

TABLE OF CONTENT ART